

Fermi surfaces of surface states on Si(111)-Ag, Au

J. N. Crain,¹ K. N. Altmann,¹ C. Bromberger,² and F. J. Himpsel¹

¹*Department of Physics, UW-Madison, 1150 University Avenue, Madison, Wisconsin 53706*

²*Department of Physics and Center for Material Science, Philipps University, D-35032 Marburg, Germany*

(Received 3 May 2002; revised manuscript received 30 July 2002; published 1 November 2002)

Metallic surface states on semiconducting substrates provide an opportunity to study low-dimensional electrons decoupled from the bulk. Angle resolved photoemission is used to determine the Fermi surface, group velocity, and effective mass for surface states on Si(111) $\sqrt{3}\times\sqrt{3}$ -Ag, Si(111) $\sqrt{3}\times\sqrt{3}$ -Au, and Si(111) $\sqrt{21}\times\sqrt{21}$ -(Ag+Au). For Si(111) $\sqrt{3}\times\sqrt{3}$ -Ag the Fermi surface consists of small electron pockets populated by electrons from a few % excess Ag. For Si(111) $\sqrt{21}\times\sqrt{21}$ -(Ag+Au) the pockets increase their size corresponding to a filling by three electrons per unit cell. The $\sqrt{21}\times\sqrt{21}$ superlattice leads to an intricate surface umklapp pattern and to minigaps of 110 meV, giving an interaction potential of 55 meV for the $\sqrt{21}\times\sqrt{21}$ superlattice.

DOI: 10.1103/PhysRevB.66.205302

PACS number(s): 73.20.At, 79.60.Jv, 73.25.+i

I. INTRODUCTION

Metallic surface states on semiconductors are special because they are the electronic equivalent of a two-dimensional electron gas in free space. Electronic states at the Fermi level E_F are purely two-dimensional since there are no bulk states inside the gap of the semiconductor that they can couple to. The states near E_F are particularly interesting because they determine most electronic properties, such as conductivity, superconductivity, magnetism, and charge density waves. Recent reports include the effects of charge density waves,¹⁻³ a two-dimensional plasmon in a metallic surface-state band,⁴ increased surface conductivity via adatom doping,⁵ and metallic umklapp bands arising from a discommensurate overlayer.⁶ In particular, surface conductivity is receiving increased interest with the arrival of sophisticated microprobes, such as four-point scanning tunneling microscopy (STM) probes.⁷⁻¹¹

Therefore, we have set out to explore the Fermi surfaces that characterize such two-dimensional states using angle-resolved photoemission with an energy resolution better than the thermal broadening of the Fermi edge ($3.5k_B T$). Angular multi detection allows us to cover \mathbf{k} space with a very fine grid and to resolve electron pockets containing as little as a few percent of an electron per surface atom. That makes it possible to explore the origin and the character of the bands that make the surface metallic. A complex array of Fermi surfaces is observed which the superlattice forms via surface umklapp.

Metallic surfaces are uncommon on semiconductors, but several structures of noble metals on Si(111) have been discovered recently that are clearly metallic. Here we focus on two-dimensional structures, i.e., Si(111) $\sqrt{3}\times\sqrt{3}$ -Ag, Si(111) $\sqrt{3}\times\sqrt{3}$ -Au, Si(111) $\sqrt{21}\times\sqrt{21}$ -(Ag+Au). Other surfaces with one-dimensional features have been explored separately.¹²⁻¹⁴

II. EXPERIMENT

First we will describe calibration of the Au and Ag coverages by low-energy electron diffraction (LEED) and the

optimum annealing sequences. The technical details of the photoemission experiment will be described at the end of this section.

Evaporators were calibrated by observing LEED images at a range of coverages on Si(111) and comparing to optimal coverages following the sequence 7×7 , 5×2 , $\alpha\text{-}\sqrt{3}\times\sqrt{3}$, $\beta\text{-}\sqrt{3}\times\sqrt{3}$ for Au, and 7×7 , $\sqrt{3}\times\sqrt{3}$ for Ag. Our LEED observations (not shown) are in line with previous work.^{15,16} As definition for the Ag and Au coverages we use units of Si(111) atomic layers (1 ML = 7.8×10^{14} atoms/cm²). The Si(111) $\sqrt{3}\times\sqrt{3}$ -Ag structure exists near 1 monolayer Ag coverage. Deposition of over 1 monolayer at 500 °C followed by subsequent post-annealing at 500 °C ensures complete coverage with no residual Si(111) 7×7 or Si(111) 3×1 -Ag, that occur below the optimum coverages. Extended annealing removes additional Ag adatoms that are present in a typical preparation.¹⁷ The Si(111) $\sqrt{3}\times\sqrt{3}$ -Au surface comes in several varieties, $\alpha\text{-}\sqrt{3}\times\sqrt{3}$ at about 0.9 monolayer coverage, $\beta\text{-}\sqrt{3}\times\sqrt{3}$ at greater than 1.0 monolayer, and 6×6 at 1.1 monolayer. The coverage phase diagrams for the $\beta\text{-}\sqrt{3}\times\sqrt{3}$ and 6×6 overlap and the preparation of the $\beta\text{-}\sqrt{3}\times\sqrt{3}$ differs only in a fast quench from 700 °C as opposed to a gradual cooling for 6×6 . All three reconstructions exhibit the same basic $\sqrt{3}\times\sqrt{3}$ diffraction spots only with different surrounding fine structure spots. In our study we focus on the β and α phases. Both are formed at a large range of annealing temperatures. In order to study a range of intermediate coverages we first deposited a high coverage (1.2 monolayers) and then gradually annealed off Au at 930 °C which is close to the Au desorption temperature. The mixed Si(111) $\sqrt{21}\times\sqrt{21}$ -(Ag+Au) surface was obtained by evaporating ~ 0.2 monolayer Au at room temperature on top of the Si(111) $\sqrt{3}\times\sqrt{3}$ -Ag surface. We find little change in the photoemission for coverages within ± 0.04 ML of the optimum. That is consistent with the observed phase separation into $\sqrt{3}\times\sqrt{3}$ -Ag and $\sqrt{21}\times\sqrt{21}$ -(Ag,Au).¹⁶

Fermi surfaces and band dispersions were acquired at 200 K with a hemispherical Scienta photoelectron spectrometer equipped with angle and energy multidetection. It was

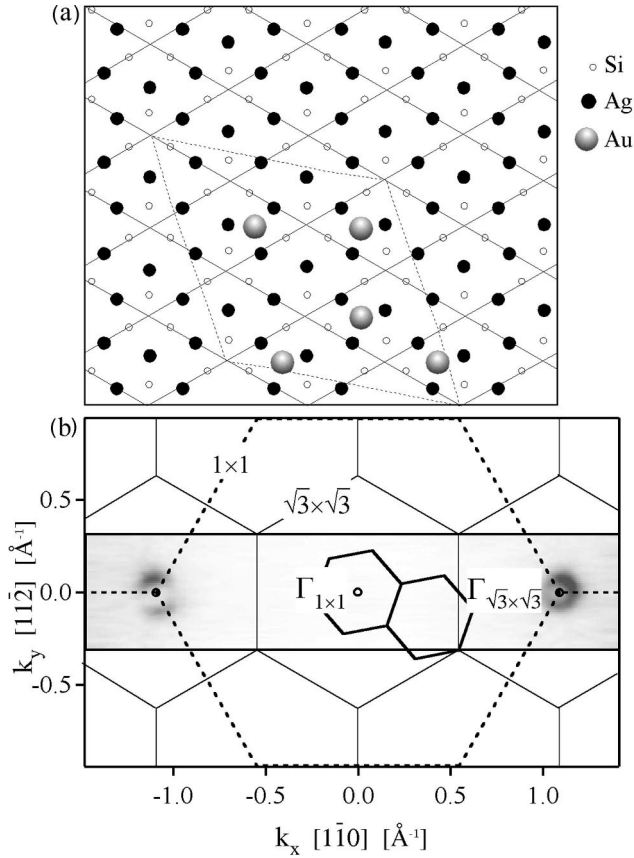


FIG. 1. Two-dimensional surface structures of Ag and Au on Si(111) in real and reciprocal space. (a) Structural models of Si(111) $\sqrt{3} \times \sqrt{3}$ -Ag and Si(111) $\sqrt{21} \times \sqrt{21}$ -(Ag+Au). The latter is obtained by adding $5/21=0.24$ monolayer Au to the $\sqrt{3} \times \sqrt{3}$ -Ag surface. (b) Surface Brillouin zones for the Si(111) 1×1 , $\sqrt{3} \times \sqrt{3}$, and $\sqrt{21} \times \sqrt{21}$ structures. The experimental Fermi surface of Si(111) $\sqrt{3} \times \sqrt{3}$ -Ag is superimposed, which consists of two small circles around the $\Gamma_{\sqrt{3} \times \sqrt{3}}$ points at $k_x = \pm 1.1 \text{ \AA}^{-1}$.

coupled to a 4 m normal-incidence monochromator at the Synchrotron Radiation Center (SRC) in Madison. The photon energy $h\nu = 34 \text{ eV}$ was selected, which gave the optimum cross section for surface states in previous work on clean Si(111) and Si(111)-Au.¹⁸ The energy resolution was 29 meV for the photons and 27 meV for the electrons. The light was p polarized with the plane of incidence along the $[1\bar{1}0]$ azimuth (horizontal in Figs. 1–5). The polar angle between photons and electrons was 50° . The polar emission angle of the photoelectrons was varied in steps of 0.5° by rotating the sample with the analyzer staying fixed. This rotation corresponds to the long, horizontal axis of our Fermi surface plots in Figs. 1–5, which is the $[1\bar{1}0]$ component of \mathbf{k}^\parallel . The perpendicular $[11\bar{2}]$ direction was covered by multidetection over a 12° range with the data points 0.24° apart. Scans were taken with an energy window of about 1 eV in 0.005 eV steps.

In this fashion we acquire the photoemission intensity in a three-dimensional parameter space, i.e., the energy E and the two in-plane k components $k_{[1\bar{1}0]}$ and $k_{[11\bar{2}]}$. By taking

slices at a constant energy $E = E_f$ we plot the Fermi surfaces (Figs. 1–5). Cuts at constant $k_{[1\bar{1}0]}$ map E versus k dispersions along $[11\bar{2}]$ (Figs. 6, 7). The original coordinates are the polar angle $\vartheta_{[1\bar{1}0]}$ and the multidetection angle $\vartheta_{[11\bar{2}]}$. These angles are converted to their corresponding parallel wave vectors according to

$$\mathbf{k}_x = \mathbf{k}_{[1\bar{1}0]}^\parallel = \hbar^{-1}(2mE_{\text{kin}})^{1/2} \cos \vartheta_{[11\bar{2}]} \sin \vartheta_{[1\bar{1}0]}$$

and

$$\mathbf{k}_y = \mathbf{k}_{[11\bar{2}]}^\parallel = \hbar^{-1}(2mE_{\text{kin}})^{1/2} \sin \vartheta_{[11\bar{2}]}.$$

Here $\vartheta_{[11\bar{2}]}$ is always smaller than $\pm 6^\circ$, and for simplicity we use the approximation $\cos \vartheta_{[11\bar{2}]} \approx 1$ in Figs. 1–5 with an error $< 1\%$.

The individual scans were normalized according to a procedure outlined in a previous report.¹⁸ Before measurement, the alignment and angular transmission function of the multidetector were carefully adjusted to provide homogeneous intensity across the 12° angular range. Any residual inhomogeneities are removed by taking an additional set of reference scans at the same spectrometer settings as the data, but with an 8 eV higher photon energy. At this energy we expect to see only secondary electrons with little angular dependence. The reference scans are integrated over energy and then used to divide out the transmission function in the raw data. Each scan, including references, is normalized to the beam current to account for the steady decline in the incident photon flux. The areal photon density within the acceptance spot of the spectrometer changes slowly with the angle of incidence of the light, causing a slow variation in the intensity that is roughly proportional to $\cos \vartheta$. The intensity of each scan was adjusted to account for this factor.

Our geometry allows us to cover most of the 1×1 surface Brillouin zone and nearly three $\sqrt{3} \times \sqrt{3}$ zones [Fig. 1(b)], with a grid dense enough to resolve fine structure within the small $\sqrt{21} \times \sqrt{21}$ Brillouin zone [Fig. 2(c)]. Even though the $E(\mathbf{k})$ band dispersions along the k_x and negative k_x directions are symmetric, the photon polarization is not. Along k_x the component perpendicular to the surface dominates, whereas along negative k_x the in-plane component dominates. That allows us conclusions about the symmetry of the surface states using polarization selection rules.

In Fig. 1 we plot a variety of unit cells together, both in real space (top) and reciprocal space (bottom). The real space $\sqrt{3} \times \sqrt{3}$ schematic is of the HCT model for Ag.¹⁹ The extra Au atoms show a possible model for the Si(111) $\sqrt{21} \times \sqrt{21}$ -(Ag+Au) surface that is consistent with recent x-ray diffraction data.^{16,20} The structure for the $\sqrt{3} \times \sqrt{3}$ Au- α phase is similar to that of the $\sqrt{3} \times \sqrt{3}$ Ag (for the differences see Refs. 21–23). The wave vectors of the various symmetry points are $\bar{K}_{1 \times 1} = 2\sqrt{2/3} \cdot 2\pi/a = 1.09 \text{ \AA}^{-1}$; $\bar{M}_{1 \times 1} = \sqrt{2}/\sqrt{3} \cdot 2\pi/a = 0.95 \text{ \AA}^{-1}$; $\bar{K}_{\sqrt{3} \times \sqrt{3}} = 0.63 \text{ \AA}^{-1}$; $\bar{M}_{\sqrt{3} \times \sqrt{3}} = 0.55 \text{ \AA}^{-1}$. The reciprocal lattice points of the $\sqrt{21} \times \sqrt{21}$ structure correspond to the center of the circles in Fig. 3(c).

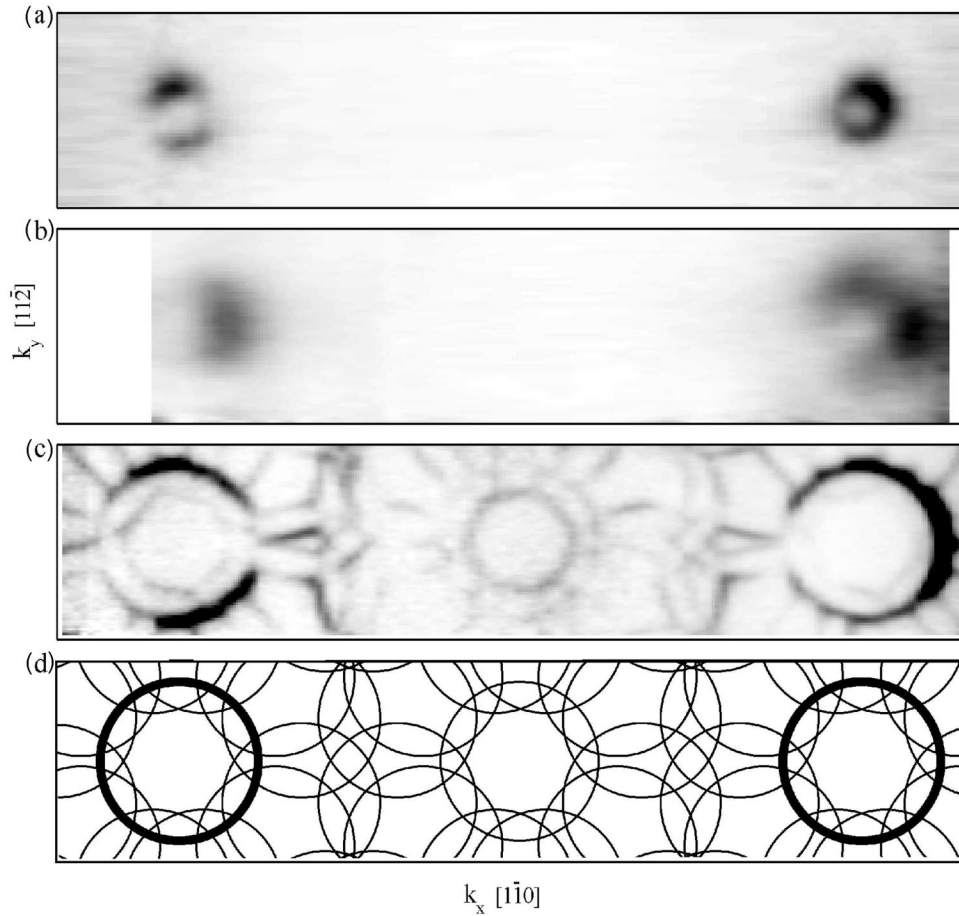


FIG. 2. Two-dimensional Fermi surface (= lines) obtained from the photoemission intensity at E_F . High intensity is shown dark, $\mathbf{k} = 0$ is at the center of each frame (compare Fig. 1). The electric field vector \mathbf{E} is close to the x direction on the left and close to the z direction on the right. (a) $\text{Si}(111)\sqrt{3}\times\sqrt{3}\text{-Ag}$ exhibits two small electron pockets around the $\Gamma_{\sqrt{3}\times\sqrt{3}}$ points due to doping with excess Ag. The circle on the left is split by a node in intensity due to polarization selection rules. (b) $\text{Si}(111)\alpha\text{-}\sqrt{3}\times\sqrt{3}\text{-Au}$ exhibits two small electron pockets similar to those with Ag. The node is missing, indicating different symmetry. (c) $\text{Si}(111)\sqrt{21}\times\sqrt{21}\text{-(Ag,Au)}$ exhibits large Fermi circles related to electrons donated by the extra Au. A horizontal intensity node indicates a band similar to $\text{Si}(111)\sqrt{3}\times\sqrt{3}\text{-Ag}$. The starting $\text{Si}(111)\sqrt{3}\times\sqrt{3}\text{-Ag}$ was stoichiometric with no excess Ag. (d) Schematic of (c) obtained by shifting the bold circles by reciprocal lattice vectors of the $\sqrt{21}\times\sqrt{21}$ structure (surface umklapp).

III. FERMI SURFACES AND BAND DISPERSION

This section presents the Fermi surfaces in Figs. 2–5 and the $E(\mathbf{k})$ band dispersions in Figs. 6, 7 for each of the three surfaces studied. The bands are mapped along the k_y direction ($= [1\bar{1}\bar{2}]$) using angular multidetection, which allows us to resolve small Fermi surfaces and band gaps.

A. $\text{Si}(111)\sqrt{3}\times\sqrt{3}\text{-Ag}$

Figures 1(b) and 2(a) map the Fermi surface for $\text{Si}(111)\sqrt{3}\times\sqrt{3}\text{-Ag}$ with excess Ag, using an energy integration interval of ± 0.025 eV around E_F . (The stoichiometric surface is semiconducting.¹⁷) High photoemission intensity is shown dark. The $\sqrt{3}\times\sqrt{3}$ Fermi surface consists of a single circle of radius $k = 0.076 \text{ \AA}^{-1}$ that is centered at the extra $\sqrt{3}\times\sqrt{3}$ Γ points [Fig. 1(b)]. The 1×1 Γ point at $k = 0$ exhibits no detectable trace of an equivalent circle, in agreement with a previously identified surface state labeled S_1 .^{24–27} Most of the unmapped portions of the first 1×1 Brillouin zone can be inferred by symmetry.

Previous photoemission reports on the $\text{Si}(111)\sqrt{3}\times\sqrt{3}\text{-Ag}$ surface have painted a complicated picture of polarization dependent effects.^{24,26,28} By mapping the entire Fermi surface in 2D instead of just a single line, we derive a more complete picture of these matrix-element effects. In Figs. 1(b), 2(a) one observes an asymmetry between positive and negative k_x that is due to polarization dependent effects. For negative k_x the angle of incidence of the light is nearly normal ($\theta_i = 27^\circ, k = -1.09 \text{ \AA}^{-1}$) and the resulting polarization vector is in the plane of the sample along $[1\bar{1}0]$. In this case the emission intensity has a node in the x direction. This matrix element effect agrees with the original findings²⁶ while recent work²⁸ finds that the metallic surface state S_1 exhibits no measurable polarization dependence. This can perhaps be understood because of the narrowness of the missing intensity around the k_x symmetry line in Fig. 2. A deviation of only a few degrees from the $(\bar{1}\bar{1}2)$ plane might disguise the polarization dependence. Reference 28 also reports that the S_1 state is excited only by the component of the

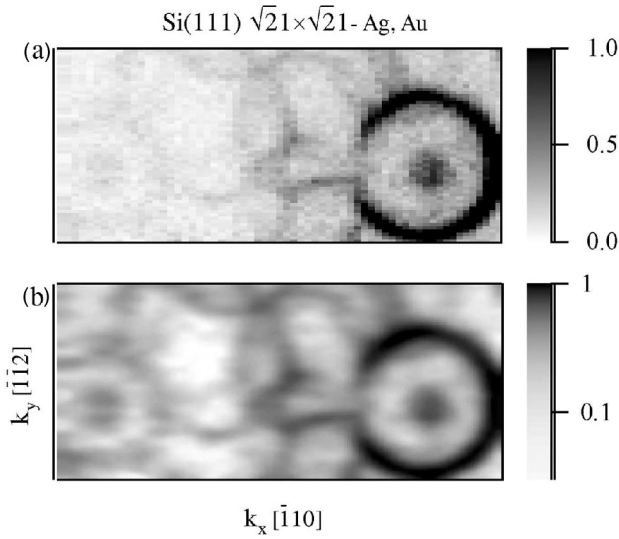


FIG. 3. Energy surface at $E_F - 0.1$ eV for $\text{Si}(111)\sqrt{21}\times\sqrt{21}-(\text{Ag}+\text{Au})$, using a starting surface with excess Ag. The small electron pocket of the $\sqrt{3}\times\sqrt{3}$ -Ag substrate (dark dot) is surrounded by a large, dark circle originating from the electrons of the additional Au atoms. Fainter circles originate from surface umklapp. (a) Raw data with high photoemission intensity shown dark. (b) Smoothed data on a logarithmic gray scale, showing fainter umklapp features.

photoelectric vector parallel to the surface, i.e., the state consists mainly of p_x and p_y components.^{24,28} However, we clearly observe the state for grazing incidence of the light [$\theta_i = 73^\circ$ corresponds to $k_x = 1.09 \text{ \AA}^{-1}$ in Fig. 2(a)] with the polarization nearly perpendicular to the surface. This apparent discrepancy is likely due to the different photon energies used, 21.2 and 34 eV, respectively. Past studies have found that the perpendicular components of surface states on Si(111) and on Si(111) with noble metal adsorbates are excited preferentially at 34 eV and are much weaker at 21 eV.^{12,13,18,29} Thus it is not surprising that in previous studies at 21.2 eV the surface state was hardly visible for grazing incidence of the light.

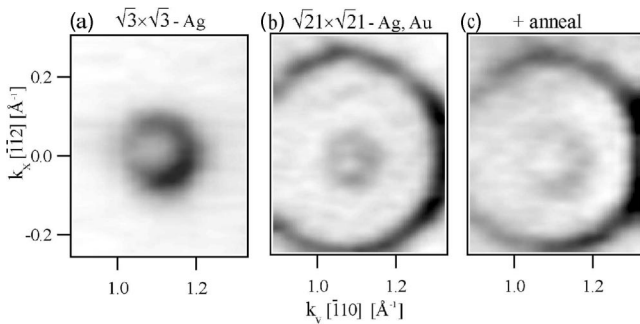


FIG. 4. Close-up of the Fermi surface around the $\Gamma_{\sqrt{3}\times\sqrt{3}}$ point (compare Fig. 1). (a) $\text{Si}(111)\sqrt{3}\times\sqrt{3}$ -Ag with a coverage slightly larger than a monolayer, giving rise to small electron pockets for the excess electrons. (b) After depositing 0.2 monolayer Au onto (a) to produce $\text{Si}(111)\sqrt{21}\times\sqrt{21}-(\text{Ag}+\text{Au})$. (c) After annealing (b) to 300 °C for 20 sec. The central Ag-induced pocket widens to its original size.

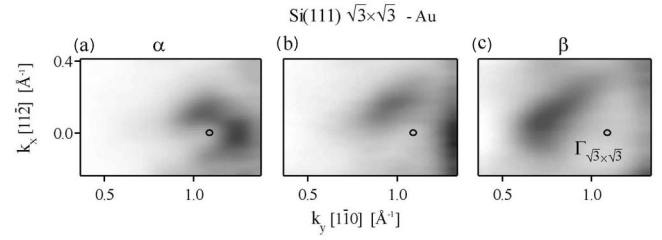


FIG. 5. The Fermi surface for $\text{Si}(111)\sqrt{3}\times\sqrt{3}$ -Au with the coverage increasing from (a) to (c). A continuous opening of the pocket at $\Gamma_{\sqrt{3}\times\sqrt{3}}$ is observed from the α phase in (a) to the β phase in (c).

B. $\text{Si}(111)\sqrt{21}\times\sqrt{21}-(\text{Ag}+\text{Au})$

The evaporation ~ 0.2 ML of additional Au onto the stoichiometric $\sqrt{3}\times\sqrt{3}$ -Ag surface yields a $\text{Si}(111)\sqrt{21}\times\sqrt{21}-(\text{Ag}+\text{Au})$ superstructure that exhibits a much larger Fermi surface due to the extra electrons provided by the Au.

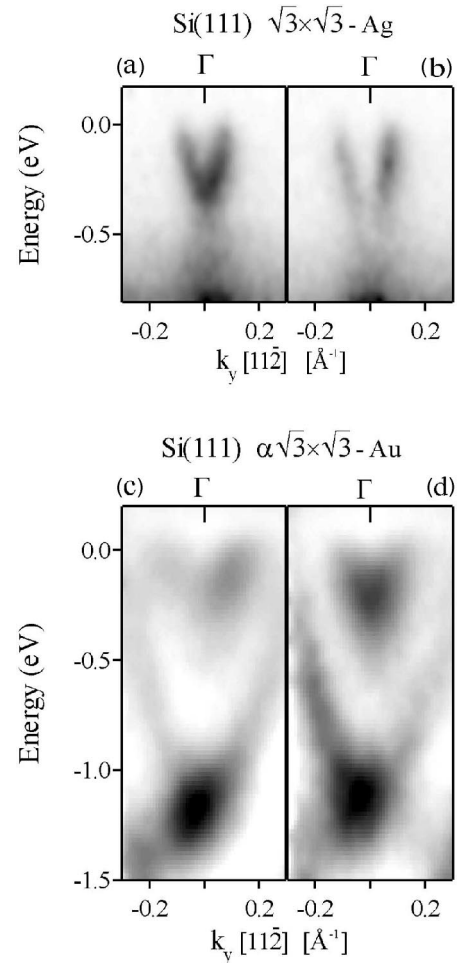


FIG. 6. $E(\mathbf{k})$ band dispersions obtained by multidetection (high photoemission intensity is dark; $E_F = 0$). All panels are cuts along k_y through the pockets at $\Gamma_{\sqrt{3}\times\sqrt{3}}$ (see Fig. 1). (a) $\text{Si}(111)\sqrt{3}\times\sqrt{3}$ -Ag for $k_x = 1.1 \text{ \AA}^{-1}$. (b) $\text{Si}(111)\sqrt{3}\times\sqrt{3}$ -Ag for $k_x = -1.1 \text{ \AA}^{-1}$, showing the node at $k_y = 0$. (c) $\text{Si}(111)\alpha\text{-}\sqrt{3}\times\sqrt{3}$ -Au for $k_x = +1.1 \text{ \AA}^{-1}$. The outer band does not reach the Fermi level. (d) $\text{Si}(111)\alpha\text{-}\sqrt{3}\times\sqrt{3}$ -Au for $k_x = -1.1 \text{ \AA}^{-1}$. The node at $k_y = 0$ is absent.

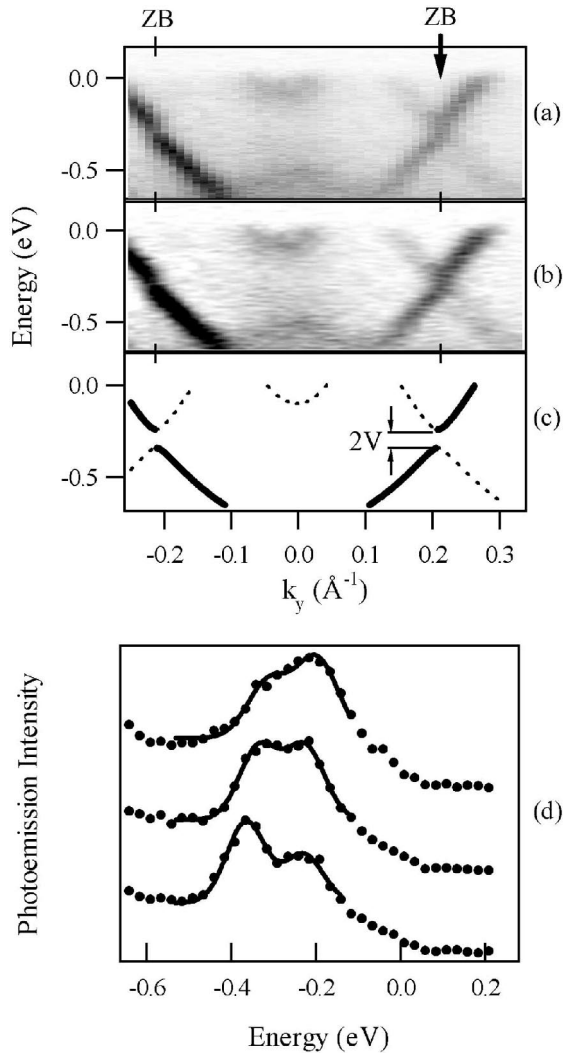


FIG. 7. $E(\mathbf{k})$ band dispersions for $\text{Si}(111)\sqrt{21}\times\sqrt{21}\text{-(Ag+Au)}$ showing minigaps induced by the $\sqrt{21}\times\sqrt{21}$ superlattice potential V . The strong outer band produces the intense Fermi circles in Figs. 2(c), 2(d), and 3. Faint $\sqrt{21}\times\sqrt{21}$ umklapp bands form avoided crossing at the zone boundary (ZB). (a) Raw data. (b) Smoothed data on a logarithmic gray scale, showing fainter umklapp features and a small central pocket from excess Ag. (c) Two band model using a $\sqrt{21}\times\sqrt{21}$ interaction potential $V=55$ meV. (d) Energy distributions corresponding to vertical cuts in (a) at the zone boundary ZB (middle curve) and on either side of it (top, bottom).

It is shown in Fig. 2(c) with an energy integration interval of ± 0.012 eV around E_F . The two strongest features are dark circles on the right and left that are located at the same Γ points as the two small circles for $\sqrt{3}\times\sqrt{3}\text{-Ag}$ in Fig. 2(a). They also exhibit the same polarization dependence with a horizontal node across the circle on the left and a nearly full circle on the right. Such similarities suggest that the same band is filled in both cases but with more electrons in the case of Au.

In addition to these main features, there are faint replicas of the Fermi circles which occur on a $\sqrt{21}\times\sqrt{21}$ reciprocal lattice, as indicated in Fig. 2(d). The resulting pattern of

circles is obtained by translating the strongest outer circle by reciprocal lattice vectors of the $\sqrt{21}\times\sqrt{21}$ lattice, i.e., via surface umklapp. In addition to the unit cell shown in Fig. 1(a) there is a second (mirror) domain rotated by an angle of 21.8° ,²⁵ which has been included in Fig. 2(d). The result is in excellent agreement with the experimental Fermi surface. The umklapp features have much lower intensity than the original circle, and there is a rapid decrease in intensity away from the two $\sqrt{3}\times\sqrt{3}\Gamma$ points. A similar effect has been observed in LEED from $\text{Si}(111)\sqrt{21}\times\sqrt{21}\text{-(Ag+Au)}$ where the $\sqrt{21}\times\sqrt{21}$ spots surrounding the $\sqrt{3}\times\sqrt{3}$ spots have much stronger intensity than those surrounding the integer order spots.¹⁶ We might expect similar effects to be observed in photoemission since it is a time-reversed LEED process.

If Au is deposited onto the Ag rich $\sqrt{3}\times\sqrt{3}\text{-Ag}$ surface an additional electron pocket is observed at the center of the large Au-induced circle. This situation is shown in Fig. 3(a) (at $E_F-0.1$ eV) and in Fig. 4(b) (at E_F) with an energy integration interval of ± 0.025 eV. The central pocket is reminiscent of the Fermi surface for Ag rich $\sqrt{3}\times\sqrt{3}\text{-Ag}$ [compare Fig. 2(a)]. A more detailed comparison can be seen in Fig. 4. Also, the polarization dependence of the small pocket (not shown) is identical to that on $\sqrt{3}\times\sqrt{3}\text{-Ag}$, indicating that it has the same origin. Our best interpretation of the two superimposed Fermi surfaces is a separation of the $\sqrt{3}\times\sqrt{3}\text{-Ag}$ phase with the $\sqrt{21}\times\sqrt{21}\text{-(Ag+Au)}$ phase. The two phases have been shown to coexist by STM.¹⁶ Once more surface umklapp generates faint circles throughout the rest of the Brillouin zone. As compared to the stoichiometric Ag preparation these bands are less distinct, and the Fermi surface is re-plotted using a logarithmic scale in Fig. 3(b) to better observe them.

In contrast to the large Fermi circle, the small central pocket is not replicated by the $\sqrt{21}\times\sqrt{21}$ [compare Figs. 2(c) and 3]. The only umklapp of the small pocket that does appear is at the $1\times 1\Gamma$ point which corresponds to a shift by a $\sqrt{3}\times\sqrt{3}$ reciprocal lattice vector.

Comparing our data to the literature elucidates why the central electron pocket is not always observed. Some photoemission studies of $\text{Si}(111)\sqrt{21}\times\sqrt{21}\text{-(Ag+Au)}$ have reported two bands^{24,30} consistent with the two Fermi circles we observe for excess Ag [Fig. 4(b)] (for the band dispersions see Fig. 7). However, in other studies the central pocket was absent,^{24,31} similar to our stoichiometric Ag preparation [Fig. 2(c)]. We attribute this difference to the presence or absence of excess Ag in the initial preparation of $\sqrt{3}\times\sqrt{3}\text{-Ag}$. Indeed, the similarity of the inner Fermi surface of Figs. 4(c) to 4(a) suggests that the inner pocket of $\sqrt{21}\times\sqrt{21}\text{-(Ag+Au)}$ is actually a vestige of the initial $\sqrt{3}\times\sqrt{3}\text{-Ag}$ surface.

Since the outer Fermi circle is directly linked to the extra Au atoms, simple electron counting arguments can be used to test the stoichiometry of Au and the number of bands in the $\sqrt{21}\times\sqrt{21}$ unit cell. The radius of the Fermi surface is $k = 0.26 \pm 0.01 \text{\AA}^{-1}$ which means that the circle subtends an area of $\pi \times (0.26 \text{\AA}^{-1})^2 = 0.21 \pm 0.01 \text{\AA}^{-2}$. This is 0.069 times the area of the 1×1 Brillouin zone (3.09\AA^{-2}) and

1.44 times the area of the $\sqrt{21} \times \sqrt{21}$ Brillouin zone. This area corresponds to 2.9 ± 0.2 electrons per $\sqrt{21} \times \sqrt{21}$ unit cell using Luttinger's theorem and assuming a single band containing electrons with both spins. A recent x-ray diffraction study²⁰ and a STM study¹⁶ support a model with 5 Au atoms per $\sqrt{21} \times \sqrt{21}$ unit cell as shown in Fig. 1(a). Since each Au atom contributes one unpaired s,p electron we can compare the number of electrons with the model Au coverage. The observed extra band can only accommodate three of the five electrons in a naive single band interpretation. Clearly, one has to go beyond that. We can think of three possible scenarios. A pair of degenerate bands could accommodate six electrons. Alternatively, an extra, filled band at lower energy would provide two additional electrons and thus accommodate a total of five electrons. The second option clearly appears closer to the experimental coverage, although we cannot completely rule out a third option where only three extra Au atoms are contained in the $\sqrt{21} \times \sqrt{21}$ unit cell.

The band dispersion for the Si(111) $\sqrt{21} \times \sqrt{21}$ -(Ag + Au) surface is shown in Figs. 7(a), 7(b) together with a model calculation in (c). The umklapp bands show up as faint lines in (a) and (b) and are represented as dashed lines in (c). An additional dashed parabola represents the central pocket left over from the $\sqrt{3} \times \sqrt{3}$ -Ag starting surface. The Brillouin zone boundary of the $\sqrt{21} \times \sqrt{21}$ lattice is at $k_y = 0.210 \text{ \AA}^{-1}$, which coincides with the intersection of the strong primary bands with the umklapp bands. The band dispersion deviates from a straight line, showing a vertical displacement at the zone boundary. This distortion can be explained by a minigap induced by the periodic potential of the $\sqrt{21} \times \sqrt{21}$ lattice. The gap can be quantified using the energy distribution curves in Fig. 7(d), which are vertical cuts in Figs. 7(a) for three momenta close to the zone boundary ZB. The bands avoid crossing each other and form a double peak with equal intensities right at the zone boundary, instead of a single peak [Fig. 7(d) middle]. After determining the peak positions from a fit with constrained, equal widths for all curves we find a gap energy $E_g = 110 \text{ meV}$. It is directly related to an interaction potential $U = E_g/2 = 55 \text{ meV}$. A similar gap was observed for Si(111) $\sqrt{21} \times \sqrt{21}$ -Ag in Ref. 31.

C. Si(111) $\sqrt{3} \times \sqrt{3}$ -Au

In Fig. 2(b) the Fermi surface for Si(111) $\alpha\sqrt{3} \times \sqrt{3}$ -Au is plotted. The region in k space is identical as for that of the $\sqrt{3} \times \sqrt{3}$ -Ag allowing for direct comparison. As with the Ag, the Fermi surface of $\alpha\sqrt{3} \times \sqrt{3}$ -Au has a single pocket centered at the $\sqrt{3} \times \sqrt{3}\Gamma$ point. This corresponds to a metallic surface state reported in earlier photoemission and inverse photoemission studies.^{29,32,33,34} The exact shape of the Fermi surface is difficult to determine because of its asymmetry across the Γ point in both the x and y directions, and the general broadness of the band. These asymmetries must be related to the dipole matrix element.

Of the Si(111) $\sqrt{3} \times \sqrt{3}$ -Au family of phases, the α phase is most similar to $\sqrt{3} \times \sqrt{3}$ -Ag. Both occur near 1 ML of coverage (0.9 ML for Au) and have some similarity in LEED

and STM. However, x-ray diffraction studies of the $\alpha\sqrt{3} \times \sqrt{3}$ Au reveal a conjugate honeycomb-chained-trimer structure (CHCT) that represents a reversal of the silicon and noble metal atoms as compared to the honeycomb-chained-trimer structure (HCT) for $\sqrt{3} \times \sqrt{3}$ -Ag.²¹⁻²³ At higher Au coverages the more complicated $\beta\sqrt{3} \times \sqrt{3}$ begins to form. STM results have demonstrated a continuous transition between the α and β phases, with the addition of Au observed as an increased density of domain walls. Various structural models have been proposed,^{35,36} but for the purposes of this paper it is sufficient to note that Si(111) $\sqrt{3} \times \sqrt{3}$ -Au is able to accommodate a large range of Au coverages in a continuous fashion.

Observations of the Fermi surface as a function of the Au coverage demonstrate the continuous filling of an electron pocket with increased Au coverage. In Fig. 5 we map the Fermi surface near the $\sqrt{3} \times \sqrt{3}\Gamma$ point for three different coverages of Au. Figure 5(a) corresponds to 0.9 ML Au (α phase), Fig. 5(c) corresponds to 1.2 ML (β phase), and Fig. 5(b) corresponds to an intermediate coverage. The size of the pocket at the Γ point increases as a function of the Au coverage. The increase in area is attributed to the addition of electrons to the unit cell accompanying the extra Au. The band also becomes very broad, especially for the intermediate Au coverage, which is consistent with the lack of long-range order observed by STM for the higher Au coverages.

IV. DISCUSSION

For the Si(111) $\sqrt{3} \times \sqrt{3}$ -Ag surface the data in Figs. 1(b), 2(a) provide two main pieces of information. The area of the Fermi surface gives the band filling (Table I). The strong dependence of the photoemission intensity from one Brillouin zone to the next and its polarization dependence are related to the wave function symmetry.

The filling of the surface state band was attributed to excess Ag in a recent core level and ARPES study on Si(111) $\sqrt{3} \times \sqrt{3}$ -Ag. It was found that the surface state band is empty at the optimum Ag coverage of 1 monolayer (ML).¹⁷ The surface state band became filled when additional Ag atoms were present in small quantities beyond the stoichiometric coverage. Our preparation, in which more than 1 ML of Ag is deposited and the excess is annealed off, is consistent with some filling of the surface state by excess Ag. If we assume a single band (with two spins) crossing the Fermi level, as in first principles calculations,^{22,37} the area inside the Fermi surface gives an electron count of 0.01 electrons per 1×1 unit cell, which would correspond to an excess of 0.01 monolayer Ag.

The surface state band is absent at the central Γ point, which is common to the 1×1 and $\sqrt{3} \times \sqrt{3}$ lattice [see Fig. 1(b)]. This observation is consistent with earlier work on Si(111) $\sqrt{3} \times \sqrt{3}$ -Ag.²⁶ Such behavior can be explained by coupling with bulk states at the valence band maximum, which is located at this Γ point. The other two Γ points on the left and right are characteristic of the $\sqrt{3} \times \sqrt{3}$ lattice and fall into a gap of bulk states. Surface umklapp would be required to bring bulk states from $k_{x,y} = 0$ to these two Γ points.

TABLE I. Band minimum E_0 , Fermi wave vector k_F , effective mass m_{eff} , and group velocity v_F of metallic surface states on Si(111).

Surface	E_0 (eV)	k_F (\AA^{-1})	m_{eff}	v_F (10^6 m/s)
Si(111) $\sqrt{3}\times\sqrt{3}$ -Ag ^a 1 + ε monolayer ^b Ag	-0.32	0.08	0.07	1.3
Si(111) $\sqrt{21}\times\sqrt{21}$ -(Ag+Au) ^c 1 monolayer Ag + 0.24 monolayer Au	-0.78	0.26	0.35	0.9
Si(111) $\sqrt{3}\times\sqrt{3}$ -Au α : 0.9 monolayer Au	-0.32	0.15	0.25	0.7

^aPrevious work (Ref. 24) reported $E_0 = -0.18$ eV, $k_F = 0.11 \text{\AA}^{-1}$, and $m_{\text{eff}} = 0.25$. The bottom of the band E_0 lies higher than in our work because of less additional Ag, corresponding to lower band filling. The larger effective mass is probably due to the use of energy distribution curves (EDC's), where the Fermi cutoff makes it difficult to determine the band position near E_F . In our study we use momentum distribution curves (MDC's) to determine the bands, which avoids this problem.

^b $\varepsilon \approx 0.01$ estimated from the area inside the Fermi surface, assuming a single, nondegenerate band (Refs. 19, 22, 37).

^cReference 24 reported $E_0 = -0.62$ eV and $m_{\text{eff}} = 0.29$. Here again the Au the Ag coverages are lower, explaining the higher E_0 by lower band filling. The band is highly nonparabolic (see Fig. 7).

A strong polarization dependence has been observed previously, and it is clarified in our data by observing the states in the k_x, k_y plane, not only along the k_x or k_y direction. A node is observed in the photoemission intensity along the k_x direction when the polarization vector \mathbf{E} is parallel to $x = [1\bar{1}0]$ [left side of Figs. 1(b), 2(a)]. Such a node in a high symmetry plane is reminiscent of dipole selection rules for a mirror plane, although one has to keep in mind that the $y = 0$ plane corresponds to $(\bar{1}\bar{1}2)$, which is not a mirror plane. For a mirror plane the node would indicate out-of-plane p_y orbital character because odd states can only be excited with the \mathbf{E} -vector perpendicular to the plane, as long as the emission is within the plane. The node is absent on the far right side of Figs. 1(b), 2(a), where the \mathbf{E} vector is close to z , the surface normal. Such behavior would be consistent with p_z orbital character. The effect of an \mathbf{E} -vector parallel to $y = [\bar{1}\bar{1}2]$ has been studied elsewhere.^{26,38} In this case one of the two $\sqrt{3}\times\sqrt{3}\Gamma$ points shows strong emission and the other is almost extinguished. This corresponds to a threefold emission pattern if the \mathbf{E} vector remains perpendicular to the emission plane. Such strong modulations should be able to provide incisive information about the wave function symmetry when modeled theoretically.

Si(111) $\sqrt{21}\times\sqrt{21}$ (Ag+Au) exhibits a striking Fermi surface that can be attributed to the $\sqrt{21}\times\sqrt{21}$ superlattice of adsorbed Au atoms. Replicas of the Au-induced electron pocket induced by translation with $\sqrt{21}\times\sqrt{21}$ reciprocal lattice vectors form a complex maze of Fermi surfaces. These surface umklapp features may be viewed as photoelectrons diffracted by the Au superlattice, analogous to the extra su-

perlattice spots seen in low energy electron diffraction (LEED). The superlattice is also felt in the $E(k)$ band dispersions, where it induces minigaps at the zone boundaries. These minigaps are directly correlated to the superlattice potential, thereby providing quantitative information about the interactions of the electrons with the superlattice (55 meV in this case).

The measured Fermi surface area of the Si(111) $\sqrt{21}\times\sqrt{21}$ -(Ag+Au) surface can be combined with the electron count to reveal some unexpected electronic features. The observed size of the large electron pocket can only explain three of the five electrons introduced into the $\sqrt{21}\times\sqrt{21}$ unit cell by the five adsorbed Au atoms. Assuming that the coverage model in Fig. 1 is correct,^{16,20} we would conclude that the remaining two electrons are accommodated by a second completely filled band. The extra band accommodating two more electrons could easily fit into a region of high density of states observed in the energy region between -0.9 and -1.5 eV. There are two alternative but less likely options. The electron pocket could be doubly degenerate and thus accommodate ≈ 6 electrons rather than 3. That leaves a mismatch by about one electron. Finally, there could be only three extra Au atoms in the $\sqrt{21}\times\sqrt{21}$ unit cell which is marginally compatible with our coverage.

In addition, the polarization dependence of the Si(111) $\sqrt{21}\times\sqrt{21}$ -(Ag+Au) surface state closely resembles that of the Si(111) $\sqrt{3}\times\sqrt{3}$ -Ag (Fig. 2). It appears that both arise from the same surface state, only with different levels of band filling. Maively, the large difference in effective mass might suggest different states for the two surface. However, the density of dopant atoms is much less in the case of $\sqrt{3}\times\sqrt{3}$ -Ag resulting in a decrease in the overlap as the bandwidth narrows. Assuming the interaction is similar, we would thus expect the effective mass to scale with the bandwidth.

The Si(111) $\alpha\sqrt{3}\times\sqrt{3}$ -Au phase is similar to Si(111) $\sqrt{3}\times\sqrt{3}$ -Ag, with both exhibiting electron pockets that are centered around the $\sqrt{3}\times\sqrt{3}$ Γ points that coincide with the 1×1 K points, but not at the Γ point $\mathbf{k}=0$. Likewise, adding Ag to $\sqrt{3}\times\sqrt{3}$ -Ag and Au to $\alpha\sqrt{3}\times\sqrt{3}$ -Au leads to an increase of the electron pockets which accommodates the extra electrons.

V. SUMMARY

In summary, we have used recent developments in energy and angle multidetection to map the complete, two-dimensional Fermi surfaces of several metallic surface structures induced by Ag and Au on Si(111). The results show that silicon surface states can have well-defined Fermi surfaces despite a tendency to form localized surface orbitals with correlation gaps.³⁹⁻⁴¹ The metallic states at the Fermi level are well suited to study low-dimensional electrons because they are decoupled from the bulk in an absolute band gap, and not just in certain k^{\parallel} regions as on metal surfaces.

The surface metallicity comes about by doping the surface

with excess Ag and Au atoms. Each of them contributes an excess electron into the conduction band. The highest amount of doping achieved on these surfaces is $3/21=0.14$ for $\sqrt{21}\times\sqrt{21}$ -(Ag+Au) and possibly higher for $\beta\text{-}\sqrt{3}\times\sqrt{3}$ -Au.

The extra reciprocal lattice vectors of the $\sqrt{21}\times\sqrt{21}$ superlattice form replicas of the $\sqrt{3}\times\sqrt{3}$ Fermi surface and lead to an intricate web of overlapping Fermi surfaces. The corresponding avoided crossings between surface umklapp bands can be mapped accurately enough to extract the superlattice potential acting on the surface electrons. Such a rich band topology promises interesting new ways of tailoring electronic states at semiconductor surfaces.

ACKNOWLEDGMENTS

We acknowledge D. Fick for stimulating discussions and support by the University Marburg. We are grateful to M. Bissen, G. Rogers, Ch. Gundelach, and M. Fisher for help with the experimental setup and to Kai-Ming Ho and Tzu-Liang Chan for discussions on the band calculations. Special thanks to Jens Kuntze for his experimental help. This work was supported by the NSF under Grant Nos. DMR-9704196, DMR-9815416, and DMR-0079983 and by the U.S. DOE under Contract No. DE-FG02-01ER45917. It was conducted at the SRC, which is supported by the NSF under Grant No. DMR-0084402.

- ¹J. M. Carpinelli, H. H. Weitering, M. Bartkowiak, R. Stumpf, and E. W. Plummer, *Phys. Rev. Lett.* **79**, 2859 (1997).
- ²J. M. Carpinelli, H. H. Weitering, E. W. Plummer, and R. Stumpf, *Nature (London)* **381**, 398 (1996).
- ³A. Mascaraque, J. Avila, E. G. Michel, and M. C. Asensio, *Phys. Rev. B* **57**, 14 758 (1998).
- ⁴T. Nagao, T. Hildebrandt, M. Henzler, and S. Hasegawa, *Phys. Rev. Lett.* **86**, 5747 (2001).
- ⁵S. Hasegawa and S. Ino, *Phys. Rev. Lett.* **68**, 1192 (1992).
- ⁶H. J. Neff, I. Matsuda, M. Hengsberger, F. Baumberger, T. Greber, and J. Osterwalder, *Phys. Rev. B* **54**, 235415 (2001).
- ⁷S. Hasegawa, K. Tsuchie, K. Toriyama, X. Tong, and T. Nagao, *Appl. Surf. Sci.* **162**, 42 (2000).
- ⁸S. Hasegawa, *J. Phys.: Condens. Matter* **12**, R463 (2000).
- ⁹I. Shiraki, F. Tanabe, R. Hobara, T. Nagao, and S. Hasegawa, *Surf. Sci.* **493**, 633 (2001).
- ¹⁰S. Hasegawa, X. Tong, S. Takeda, N. Sato, and T. Nagao, *Phys. Solid State* **60**, 89 (1999).
- ¹¹C. L. Petersen, F. Grey, and M. Aono, *Surf. Sci.* **377**, 676 (1997).
- ¹²R. Losio, K. N. Altmann, A. Kirakosian, J.-L. Lin, D. Y. Petrovykh, and F. J. Himpsel, *Phys. Rev. Lett.* **86**, 4632 (2001).
- ¹³R. Losio, K. N. Altmann, and F. J. Himpsel, *Phys. Rev. Lett.* **85**, 808 (2000).
- ¹⁴H. W. Yeom, S. Takeda, E. Rotenberg, I. Matsuda, K. Horikoshi, J. Schaefer, C. M. Lee, S. D. Kevan, T. Ohta, T. Nagao, and S. Hasegawa, *Phys. Rev. Lett.* **82**, 4898 (1999).
- ¹⁵T. Nagao, C. Voges, H. Pfner, M. Henzler, S. Ino, F. Shimokoshi, and S. Hasegawa, *Appl. Surf. Sci.* **132**, 47 (1998).
- ¹⁶J. Nogami, K. J. Wan, and X. F. Lin, *Surf. Sci.* **306**, 81 (1994).
- ¹⁷R. I. G. Uhrberg, H. M. Zhang, T. Balasubramanian, E. Landemark, and H. W. Yeom, *Phys. Rev. B* **65**, 081305 (2002).
- ¹⁸R. Losio, K. N. Altmann, and F. J. Himpsel, *Phys. Rev. B* **61**, 10 845 (2000).
- ¹⁹Y. G. Ding, C. T. Chan, and K. M. Ho, *Phys. Rev. Lett.* **67**, 1454 (1991).
- ²⁰H. Tajiri, K. Sumitani, W. Yashiro, S. Nakatani, T. Takahashi, K. Akimoto, H. Sugiyama, X. Zhang, and H. Kawata, *Surf. Sci.* **493**, 214 (2001).
- ²¹D. Dornisch, W. Moritz, H. Schulz, R. Feidenhansl, M. Nielsen, F. Grey, and R. L. Johnson, *Phys. Rev. B* **44**, 11 221 (1991).
- ²²Y. G. Ding, C. T. Chan, and K. M. Ho, *Surf. Sci.* **275**, L691 (1992).
- ²³J. Quinn, F. Jona, and P. M. Marcus, *Phys. Rev. B* **46**, 7288 (1992).
- ²⁴X. Tong, C. S. Jiang, and S. Hasegawa, *Phys. Rev. B* **57**, 9015 (1998).
- ²⁵X. Tong, Y. Sugiura, T. Nagao, T. Takami, S. Takeda, S. Ino, and S. Hasegawa, *Surf. Sci.* **408**, 146 (1998).
- ²⁶L. S. O. Johansson, E. Landemark, C. J. Karlsson, and R. I. G. Uhrberg, *Phys. Rev. Lett.* **63**, 2092 (1989).
- ²⁷J. Viernow, M. Henzler, W. L. O'Brien, F. K. Men, F. M. Leibsle, D. Y. Petrovykh, J. L. Lin, and F. J. Himpsel, *Phys. Rev. B* **57**, 2321 (1998).
- ²⁸X. Tong, S. Ohuchi, N. Sato, T. Tanikawa, T. Nagao, I. Matsuda, Y. Aoyagi, and S. Hasegawa, *Phys. Rev. B* **64**, 205316 (2001).
- ²⁹K. N. Altmann, J. N. Crain, A. Kirakosian, J.-L. Lin, D. Y. Petrovykh, F. J. Himpsel, and R. Losio, *Phys. Rev. B* **64**, 035406 (2001).
- ³⁰X. Tong, C. S. Jiang, K. Horikoshi, and S. Hasegawa, *Surf. Sci.* **31**, 125 (2000).
- ³¹H. M. Zhang, K. Sakamoto, and R. I. G. Uhrberg, *Phys. Rev. B* **64**, 245421 (2001).
- ³²C. J. Karlsson, E. Landemark, L. S. O. Johansson, and R. I. G. Uhrberg, *Phys. Rev. B* **42**, 9546 (1990).
- ³³J. M. Nicholls, F. Salvan, and B. Reihl, *Phys. Rev. B* **34**, 2945 (1986).
- ³⁴H. M. Zhang, T. Balasubramanian, and R. E. G. Uhrberg, *Phys. Rev. B* **66**, 165402 (2002).
- ³⁵D. Grozea, E. Landree, L. D. Marks, R. Feidenhans'l, M. Nielsen, and R. L. Johnson, *Surf. Sci.* **418**, 32 (1998).
- ³⁶E. A. Khramtsova, H. Sakai, K. Hayashi, and A. Ichimiya, *Surf. Sci.* **435**, 405 (1999).
- ³⁷Y. G. Ding, C. T. Chan, and K. M. Ho, *Phys. Rev. Lett.* **69**, 2452 (1992).
- ³⁸V. Perez-Dieste, Ph.D. thesis, Universidad Autonoma de Madrid, Madrid, 2002.
- ³⁹V. Ramachandran and R. M. Feenstra, *Phys. Rev. Lett.* **82**, 1000 (1999).
- ⁴⁰H. H. Weitering, J. Chen, N. J. Dinardo, and E. W. Plummer, *Phys. Rev. B* **48**, 8119 (1993).
- ⁴¹H. H. Weitering, X. Shi, P. D. Johnson, J. Chen, N. J. DiNardo, and K. Kempa, *Phys. Rev. Lett.* **78**, 1331 (1997).